

Evidence of subduction, collision, and extension in northern Borneo: Constraints from receiver functions

Amy Gilligan(1),* David G. Cornwell(1), Nicholas Rawllinson(2), Felix Tongkul(3), Simone Pilia(4), Tim Greenfield(2), Conor A. Bacon(5)

1. School of Geosciences, University of Aberdeen, Aberdeen, UK
2. Department of Earth Sciences, University of Cambridge, Cambridge, UK
3. Faculty of Science and Natural Resources, Universiti Malaysia Sabah, Kota Kinabalu, Malaysia
4. College of Petroleum Engineering and Geosciences, King Fahd University of Petroleum and Minerals, Dhahran, Saudi Arabia
5. Lamont-Doherty Earth Observatory, Columbia University, Palisades, New York, USA

* Corresponding author: amy.gilligan@abdn.ac.uk

Highlights

- A new Vs model for northern Borneo is obtained from P-receiver functions jointly inverted with a global surface wave model.
- Crustal thickness is found to vary from 24km beneath central northern Borneo, to 60km beneath the Crocker Range.
- We image Dangerous Grounds crustal material underthrust beneath western Sabah following subduction and collision.

Abstract

Northern Borneo (Sabah) has a complex geological history, experiencing multiple episodes of subduction, magmatism, uplift, subsidence, and extension since the Mesozoic. This includes the subduction of the proto-South China Sea beneath Sabah, terminating ~21 Ma; a postulated later phase of subduction of the Celebes Sea plate, terminating ~9 Ma; extension in central

33 Sabah ~9-10Ma; rapid emplacement and exhumation of a granite intrusion
34 ~7Ma, and the development of a fold-thrust belt offshore during the last 5 Myr.
35 While these events have left imprints in the surface rock record, it has not
36 been possible, until recently, to investigate deeper lithospheric processes that
37 have shaped Sabah. The installation of 46 broadband seismometers - the
38 northern Borneo Orogeny Seismic Survey (nBOSS) - between 2018 and 2020
39 means that it is now possible to constrain the architecture of the crust and
40 uppermost mantle beneath Sabah. We use two years of passive seismic data
41 recorded by the nBOSS network, and an additional 24 Malaysian
42 Meteorological Service broadband seismometers in Sabah to calculate P-
43 wave receiver functions. We then use these in a joint inversion with surface
44 wave data to obtain shear velocity models of crustal structure. The thickest
45 crust (60km) occurs beneath the Crocker Range, while the thinnest crust
46 (24km) is found in central Sabah, potentially recording Miocene extension.
47 The crust beneath the 4095m high Mt Kinabalu is also comparatively thin.
48 Distinct, low-velocity, dipping anomalies identified in our shear wave velocity
49 models provide clear evidence for underthrusting of Dangerous Grounds
50 continental crust following subduction and collision.

51

52 **Plain language summary**

53

54 The processes that happen because of the movement of tectonic plates leave
55 an imprint on the interior of the Earth, and to fully understand these processes
56 we need to make images of the subsurface. Over the last 65 Million years, the
57 northern part of the island of Borneo (Sabah) has been affected by multiple

58 tectonic events including potentially two episodes of subduction – where one
59 tectonic plate descends beneath the other - and mountain building due to the
60 collision between the Dangerous Grounds and Sabah. Until recently there
61 were insufficient instruments to make the measurements necessary to obtain
62 images of the interior of the Earth beneath Sabah. In 2018 this situation was
63 transformed with the installation of 46 seismometers – instruments that detect
64 earthquakes. We use the records from distant earthquakes recorded by these
65 and pre-existing seismometers to build up a picture of the Earth ~100km
66 below the surface of Sabah. Our work reveals that the thickness of the crust
67 beneath Sabah varies from 24km in central Sabah, to 60km beneath the
68 Crocker Range. We also image part of the Dangerous Grounds crust now
69 situated beneath Sabah, emplaced as a result of the collision between these
70 two tectonic blocks.

71

72

73

74 **Introduction**

75

76 Subduction is fundamental to the growth of continents (e.g. Foley et al.,
77 2002), driving plate motion (Forsyth and Uyeda, 1975), and long-term climate
78 regulation (e.g. Johnston et al., 2011). Eventually subduction will come to an
79 end (e.g., via continent-continent collision), and this may result in magmatism,
80 exhumation, rapid uplift, and subsidence (e.g. Zandt et al., 2004, Levander et
81 al., 2011, Li et al., 2016). The processes occurring in these post-subduction
82 settings remain, at present, poorly understood. Given that subduction has
83 been happening on Earth for at least 1.8 Ga (Weller and St Onge, 2017),

84 explaining post-subduction processes is vital, not just for our understanding of
85 present-day tectonics, but also for interpreting the deep geological record.

86

87 Northern Borneo is an ideal location for studying post-subduction processes.

88 It is thought to be the site of two subduction systems that have terminated

89 since the start of the Neogene: the subduction of the proto-South China Sea

90 (pSCS) until ~21 Ma (Lai et al., 2021, Hall 2013, Morley and Back, 2008,

91 Tongkul 1994, Tongkul 1991) along the present-day NW coast of Sabah, and

92 the subduction of the Celebes Sea along the present-day SE coast of Sabah,

93 which terminated ~9 Ma (Lai et al., 2021). In this study we use passive

94 seismic data recorded by a network of broadband seismometers deployed

95 across the Malaysian state of Sabah, situated on the northern end of the

96 island of Borneo, between 2018-2020 (Figure 1) to image the crust and

97 mantle lithosphere to both improve our understanding of the tectonic setting of

98 northern Borneo and provide new insight into subduction termination and

99 post-subduction processes.

100

101 ***Geology and tectonic setting of Sabah***

102

103 The diverse surface geology of Sabah is testament to the rich range of

104 tectonic processes that have affected the northern part of Borneo since the

105 Mesozoic. Some of the oldest dated rocks are those of the Segama Valley

106 Felsic Intrusions (250 and 241 Ma) (Burton-Johnson et al., 2020) in eastern

107 Sabah, which are intruded into ophiolitic rocks, with some subsequent,

108 mineralogically distinct, felsic intrusions in the same area being dated at ~178

109 Ma. It has been proposed (Burton-Johnson et al. 2020, Balaguru and Nichols,

110 2004) that these formed in an extensional basin in a suprasubduction setting,
111 which was then uplifted and eroded in the latest Cretaceous or earliest
112 Paleocene, around 66 Ma (Balaguru and Nichols, 2004). A recent study by
113 Tian et al., (2024) has dated, using Zircon U-Pb ages, ophiolites in Sabah to
114 248-244 Ma, which they argue formed in a small extensional setting related to
115 the subduction of Paleo-Tethys and the start of subduction of the Paleo-
116 Pacific plate.

117

118 By the Paleocene (66-56Ma) subduction of the proto-South China Sea
119 towards the south-east beneath what is now the western edge of Sabah had
120 begun (e.g., Hutchison et al., 2000, Rangin et al., 1999). Cumulate gabbros,
121 part of the Sabah Ophiolite, in the Tongod-Telupid area have been dated to
122 42.65 ± 0.51 Ma (Lai et al., 2021), and from their geochemical signature are
123 thought to have formed in a back-arc basin. Similarly, the geochemistry of the
124 Sandakan andesitic tuff (33.9 ± 7.7 Ma, Bergman et al., 2000) could also
125 suggest a back-arc basin setting (Lai et al., 2021, Hutchison et al., 2000). In
126 the fore-arc, thick (~9000 m) sedimentary successions of deep marine
127 sandstones, shales and minor conglomerates, are present in the NE-SW
128 trending Crocker Basin (Balaguru and Nichols, 2004).

129

130 Opening of the South China Sea (~33-32 Ma, (Franke, 2013, Barckhausen et
131 al., 2014, Li et al., 2014)), driven by subduction of the proto-South China Sea,
132 pushed continental slivers, including the Dangerous Grounds and Reed Bank
133 blocks, towards Borneo (e.g., Tongkul 1991, Tongkul 1994, Hutchison et al.,
134 2000, Hall 2013, Rangin et al., 1999). Subduction of the proto-South China

135 Sea continued in the earliest part of the Miocene (24-21 Ma, Lai et al., 2021
136 and references therein), however, at around 21 Ma the Dangerous Grounds
137 block collided with and then underthrust northern Borneo (Lai et al., 2021, Hall
138 2013, Morley and Back, 2008, Tongkul 1994, Tongkul 1991), which ultimately
139 caused subduction to cease. This collision led to uplift above sea level
140 (Burton-Johnson et al, 2020, Hall 2013, Morley and Back, 2008). However, by
141 the end of the Early Miocene, most of Sabah was at or below sea level once
142 more, with low hills where the Crocker Range is today (Hall 2013, Cottam et
143 al, 2013).

144

145 Subduction of the Celebes Sea beneath eastern Sabah began at a similar
146 time to the termination of subduction of the proto-South China Sea and may
147 have been a result of changes in regional stresses due to the Sabah-
148 Dangerous Grounds collision (Lai et al., 2021, Linang et al., 2022). In the Dent
149 Peninsular, rocks that are the product of arc magmatism have been dated to
150 18.8-17.8 Ma and in the Semporna Peninsula to 18.2-14.4 Ma (Macpherson
151 et al., 2010). It is, however, important to note that the idea that there was
152 northwards subduction of the Celebes Sea is contested (Burton-Johnson and
153 Cullen, 2023). A slab from this subduction event has yet to be imaged in the
154 mantle.

155

156 Roll-back of the Celebes Sea subduction from 19 Ma led to extension in the
157 Sulu Sea and in Sabah (Hall, 2013). Thick (~6 km) successions of
158 carbonates, shallow marine, and fluvio-deltaic sediments, including coals,
159 were deposited in a basin in Central Sabah (Tongkul and Chang, 2003,

160 Balaguru and Nichols 2004, Burton-Johnson et al., 2021). The coastal/shelf
161 environments for all these sediments, including coal that was buried to 3 km
162 depth (Balaguru and Nichols, 2004), means that subsidence must have
163 continued over a prolonged period. Tsikouras et al., (2021) argue that the
164 major increase in extension suggested by Huang (1991) between 9 and 11
165 Ma led to rifting in Ranau area, and suggest that sea-floor spreading took
166 place in the Telupid area. This is disputed by Cullen and Burton-Johnson
167 (2021) who argue that while extension took place, the Sulu Sea rift did not
168 extend into Sabah. In a recent review Lai et al., (2021) suggest that Celebes
169 Sea subduction beneath Borneo terminated ~9 Ma.

170

171 The Kinabalu pluton, which forms the 4095 m high Mt Kinabalu, was intruded
172 into peridotites and the Crocker formation between 7.85 and 7.22 Ma, at a
173 depth of 3-8 km (Cottam et al., 2013). Between 6.6 and 5.8 Ma it was rapidly
174 cooled and exhumed with rates of up to 7 mm/yr (Cottam et al., 2013). The
175 emplacement and exhumation of the Kinabalu pluton likely occurred in an
176 extensional setting (Hall et al., 2013, Burton-Johnson et al., 2019).

177

178 Sabah only became fully emergent above sea level by the end of the Miocene
179 to early Pliocene (~5 Ma), and uplift has occurred since (Roberts et al., 2018,
180 Hall 2013, Morley and Black 2008). This includes uplift of the circular basins,
181 such as the Maliau Basin, in central Sabah (Tongkul and Chang, 2003).

182 During the Pliocene large-scale gravitational collapse occurred, seen in mass
183 transport slumps, megaslides and extensional faults (Cottam et al., 2013), and
184 as result of this, a fold and thrust belt has developed offshore of western

185 Sabah (e.g., Spain et al., 2013, Franke et al., 2008, King et al., 2010). Around
186 5 Ma a change in the composition of volcanic rocks in eastern Sabah also
187 occurs from calc-alkaline to a similar composition to ocean island basalts
188 (OIB), (Macpherson et al., 2010). Volcanism in eastern Sabah has continued
189 into the Holocene, potentially as recently as 24-27 ka based on radiocarbon
190 dating of carbonised material (Kirk, 1968; Bellwood, 1988; cited in Tjia et al.,
191 1992), although Takashima et al., (2004) date the youngest volcanics in their
192 study using thermo-luminescence to 90 ka.

193

194 ***Previous geophysical work***

195

196 Regional-scale tomographic studies of South-East Asia have observed
197 anomalously high seismic velocities in the upper mantle beneath Sabah at
198 depths of ~100-300 km (e.g., Amaru, 2007, Tang and Zheng, 2013, Hall and
199 Spakman, 2015, Zenonos et al., 2019, Wehner et al., 2022). These high
200 velocities are attributed to the presence of slab remnants in the upper mantle.
201 While the earlier body-wave studies (e.g., Amaru, 2007, Hall and Spakman
202 2015, Zenonos et al., 2019) had limited resolution beneath Sabah, thus
203 bringing the existence of higher velocities into question, the full-waveform
204 model of Wehner et al., (2022), SASSY21, uses data from the same dense
205 seismic network in Borneo used in this study, and so has improved resolution
206 in this region. Other results from this dense seismic network – the nBOSS
207 network – are described below.

208

209 In a Sabah-focused P- and S-wave tomographic study, also using nBOSS
210 data, Pilia et al., (2023a), observe two distinct fast velocity anomalies in the
211 upper mantle beneath Sabah. One, an elongate anomaly at depths >250 km
212 underlying most of the Crocker Range, is attributed to the proto-South China
213 Sea Slab, while the other, a relatively narrow (<100 km) anomaly between
214 ~150 and 300 km depth in central Sabah, is interpreted to be a lithospheric
215 drip from the volcanic arc root beneath the Semporna Peninsular. Pilia et al.,
216 (2023b) perform thermo-mechanical modelling and suggest that the
217 downwelling drip can cause extension and crustal thinning, resulting in
218 melting and exhumation of sub continental material. As such, the 'Semporna
219 drip' may play an important role in the emplacement of the Kinabalu pluton, as
220 well as explaining subsidence and uplift, and the lavas with an OIB
221 composition in eastern Sabah.

222

223 Bacon et al., (2022) investigate anisotropy beneath Sabah using XKS splitting
224 measurements extracted from nBOSS teleseismic data. Their results
225 demonstrate that fossil anisotropy in the lithosphere is the main control on
226 anisotropic properties in this post-subduction setting. They observe fast
227 directions parallel to the strike of the Crocker range in western Sabah, likely
228 imparted when the Dangerous Grounds block collided with Sabah. In the east
229 of Sabah, fast directions are sub-parallel to the direction of spreading in the
230 Sulu Sea, suggesting that the anisotropic fabric may have developed as a
231 result of extension, while the null results they observe in the southeast may
232 arise due to the lithospheric drip observed by Pilia et al., (2023a).

233

234 Roberts et al., (2018) suggest that removal of the lithosphere and
235 replacement by hot asthenospheric material could explain the relatively rapid
236 uplift and erosion rates observed in Sabah (~0.1-0.3 mm/yr, Morely and Back,
237 2008). They base their estimates of thin lithosphere on regionally extensive
238 slow shear wave velocities at 100-200 km depth in the global tomographic
239 model of Schaeffer and Lebedev (2014). However, in recent 2-plane-wave
240 tomography of Sabah from Greenfield et al., (2022), average lithosphere
241 thickness beneath Sabah is found to be ~100 km, with the lithosphere only
242 being thin (<50km) beneath the Semporna Peninsula, consistent with the work
243 of Pilia et al., (2023b) that suggests that the lithosphere here has dripped off.
244

245 Until recently, estimates of crustal thickness in Sabah had been limited. Holt
246 (1998) modelled gravity data from Sabah and suggested that the whole of
247 Sabah was underlain by crust >30 km thick, that crustal thicknesses beneath
248 the Crocker Range were ~50 km, and 39 km beneath central Sabah.
249 Estimates of 27 ± 3 km and 33 ± 2 km beneath seismometers KKM and LDM
250 near Kota Kinabalu and Lahad Datu respectively have been made by Lipke
251 (2008) from H-k stacking of receiver functions, while Syuhada et al., (2022)
252 invert receiver functions from KKM and LDM using the Neighbourhood
253 algorithm and find crustal thicknesses of 30 km and 26 km, respectively. Latiff
254 and Othman (2020) invert receiver functions from KKM and find a crustal
255 thickness of 40km. A regional crustal thickness map derived from surface
256 wave data made by Tang and Zheng (2013) estimates crustal thickness
257 beneath Sabah to be 27.5-32.5 km. The deployment of the nBOSS seismic
258 network between 2018-2020 has allowed for more detailed studies of crustal

259 thickness across the whole of Sabah to be conducted. Greenfield et al.
260 (2022) use the 4.1 km/s velocity contour in their shear wave velocity model as
261 a proxy for the Moho and suggest that crustal thicknesses vary from 25-55
262 km, with the thickest crust beneath the Crocker Range and the Dent
263 Peninsula, and the thinnest crust in north east Sabah. Linang et al. (2022) use
264 Virtual Deep Seismic Sounding (VDSS) to estimate crustal thickness in the
265 range 21 - 46 km, with a similar pattern of thicker and thinner crust.

266

267 Until now, due to a lack of seismic instrumentation in the region, it has not
268 been possible to derive a detailed model of the seismic velocity structure of
269 Sabah's crust. Consequently, debates have continued to emerge (e.g.,
270 Milsom et al. 2001, Cullen and Burton-Johnson, 2021) about the nature of the
271 crust beneath this part of Borneo and the processes that have shaped it. Fone
272 et al., (2024) use data from the nBOSS network to develop an ambient noise
273 phase velocity model of the crust to 36s period, and invert their surface wave
274 data for a shear velocity model. This model is able to well resolve lateral
275 features greater than 50km well, highlighting the heterogenous nature of the
276 crust in Sabah, but is limited in its resolution of vertical contrasts.

277

278 In order to further understanding of crustal and upper mantle structure,
279 particularly vertical discontinuities, we calculate radial P-wave receiver
280 functions at 70 seismic stations, including the recent nBOSS deployment
281 across Sabah, and jointly invert these with surface wave data to develop a
282 detailed shear velocity model of the crust in Sabah, allowing us to map the

283 Moho geometry beneath. These results provide important constraints on
284 processes that have shaped the region.

285

286 **Data and Methods**

287

288 Broadband teleseismic data in this study come from two seismic networks
289 deployed in Sabah (Figure 1, Supplementary Table 1). The temporary nBOSS
290 network of 46 seismometers, installed mostly on a ~40x40 km grid , with a
291 mean interstation distance of 37.5km (Bacon, 2021), between March 2018
292 and January 2020, consisted of 18 Güralp 3ESPD instruments and 28 Güralp
293 6TD instruments (Rawlinson, 2018, Pilia et al., 2019). We also used data from
294 the Malaysian Metrological Service permanent seismic network. In Sabah, this
295 consists of 24 permanently installed Streckeisen STS2/2.5 and SS1-Ranger
296 seismometers, predominantly located in regions of elevated seismicity around
297 Mt Kinabalu and Darvel Bay.

298

299 Calculation of radial P receiver functions from 3-component seismograms of
300 teleseismic (30-90° epicentral distance) earthquakes allows us to investigate
301 the structure of the crust, including determining Moho depth and identifying
302 layering within the crust.

303

304 We performed the initial quality control of the seismograms in two stages.

305 First, a total of 27,660 3-component seismograms from March 2018-

306 September 2018 for earthquakes $M_w > 5$ that met the distance criteria were

307 visually inspected. Where the P-wave signal-to-noise ratio was high (e.g., a P

308 arrival could clearly be identified) on all 3 components, these seismograms

309 were classified as 'good' and were taken forward for further analysis. All other
310 seismograms were rejected and classified as 'bad'. Using this classified data
311 set we developed a deep learning algorithm to determine the probability of a
312 3-component seismogram being suitable for further analysis. The annotated
313 (good or bad) seismograms were converted into spectrograms and 80% of the
314 data were used to train an image classification convolutional neural network,
315 ResNet50, pretrained on ImageNet (He et al., 2016). The data classification
316 algorithm was then tested using the remaining 20 per cent of the data and had
317 a 92.7 per cent accuracy. A total of 57,858 3-component seismograms from
318 September 2018-January 2020 were then used with the classification
319 algorithm, and only those classified with a greater than 50 per cent probability
320 of being 'good' were visually inspected. This significantly reduced the time
321 needed for this stage of data quality control, while resulting in a similar
322 proportion of events being taken forward for further analysis.

323

324 After initial quality control, 14,447 seismograms were used to calculate
325 receiver functions using the time-domain iterative deconvolution method of
326 Ligorria and Ammon (1999), with a gaussian width of 1.6, corresponding to a
327 frequency of 0.9Hz. A gaussian width of 1.6 provides a good balance of
328 resolving detail in the crust, while avoiding the risk of overinterpreting noise.
329 Further quality control steps included removal of receiver functions with a poor
330 fit (<70 per cent), and those which appeared noisy, oscillatory or anomalous
331 to other receiver functions from a similar distance and backazimuth on visual
332 inspection. This left a remaining dataset of 3338 receiver functions. Eight
333 stations, one from the nBOSS network, and seven from the Malaysian

334 Metrological Service permanent seismic network, had no usable receiver
335 functions. For stations with usable receiver functions, the number of receiver
336 functions at individual seismometers ranges from 9 at SPM to 183 at SBA8
337 (Supplementary Table 1, Supplementary Figure 1). This is due to variations in
338 the amount of data available from individual stations and the noise levels at
339 the installation sites.

340

341 Receiver functions at an individual station are stacked together to reduce
342 noise, and these stacks are used in an inversion for crustal velocity structure.
343 While useful, the interpretation of receiver functions on their own is inherently
344 non-unique (Ammon et al., 1990). Therefore, to ensure that shear velocities
345 we obtain from inversions of receiver functions are realistic for this region, we
346 jointly invert the receiver functions with fundamental mode Rayleigh wave
347 group velocity dispersion curves extracted from the GDM52 global compilation
348 (Ekström, 2011) for each station location for a period range 25–250 s. This
349 model is relatively coarse ($1^\circ \times 1^\circ$), does not see much variation in group
350 velocities beneath Sabah (Supplementary Figure 2), and with a minimum
351 period of 25s, is most sensitive to depths of 25km and below, corresponding
352 to the mid to lower crust and upper mantle in this area. We are primarily
353 concerned in this study that the inversions result in velocity models that fit the
354 receiver function data.

355

356 The radial P receiver function stacks, together with the dispersion curves, for
357 each station were inverted for shear velocity structure using joint96
358 (Herrmann, 2013), an iterative linearised least squares inversion method.

359 Several starting models were tested including constant values of 4.48 km/s,
360 (mantle velocity in the ak135 model - see Kennett et al., 1995), 4.28 km/s, and
361 3.70 km/s and a V_p/V_s value of 1.74 down to 100 km depth, parameterised
362 into 2 km thick layers, overlying ak135 (Supplementary Figure 3). While there
363 are some small variations in the absolute shear velocities due to differences in
364 the starting models, they are sufficiently small to not alter the interpretation of
365 the structure. We test different relative weights (p value in joint96) of surface
366 waves to receiver function data in the inversion: 0.5, 0.1, 0.05 and 0.01.
367 Models with $p=0.5$ are smoother than those with a lower p value, reflecting the
368 greater contribution of surface wave data. Overall, the models show little
369 variation in structure with p value, indicating that the recovered features are
370 robust (Supplementary Figure 4).

371 In order to test the stability of the results, the receiver functions at each station
372 were divided into 3 time periods (March 2018-Sept 2018, Sept 2018-March
373 2019, March 2019-Jan 2020) and were stacked and inverted separately.
374 There was very little difference between the resulting models and those
375 obtained from the complete dataset (Supplementary Figure 5). This can be
376 considered a form of bootstrapping, and gives us further confidence that the
377 results are robust

378 **Results**

379

380 *Individual receiver functions*

381 Plotting individual receiver functions with respect to backazimuth (e.g
382 Supplementary Figure 1, Supplementary Figure 6), shows that for some

383 stations there is a degree of variability for events at different backazimuths.
384 There are a number of potential causes of this, including short-length scale
385 variation in crustal structure, anisotropy in the crust, and dipping layers in the
386 crust. Unfortunately the backazimuthal range of events in this study is limited,
387 with events being mainly to the north east or south east of the seismometers,
388 meaning it is not possible to model the cause of the backazimuthal variation
389 effectively. Because of this limitation, we consider all receiver functions at a
390 station in a signal stack.

391

392 At some stations we observe receiver functions that do not fit with the typical
393 idea of a receiver function, which in some automated QC approaches would
394 have been rejected. One of the most extreme examples of this are the
395 receiver functions computed for events recorded by the station SBG3
396 (Supplementary Figure 6). Here, the amplitude of the first arrival is relatively
397 low, merging with a large amplitude positive arrival at ~2. There is a large
398 amplitude negative arrival at ~4s, and a large amplitude positive arrival at ~5s.
399 At this station there are 52 individual receiver functions that have this pattern
400 (i.e all those with north easterly or south easterly backazimuths). Further, the
401 Malaysian Metrological Service seismometer PTM, located ~20km from
402 SBG3, also shows similar pattern of positive and negative arrivals. PTM is a
403 different type of seismometer, deployed in a different way to SBG3. The
404 consistency between multiple events, and similarities between receiver
405 functions at different, but relatively close, locations suggests that, while these
406 receiver functions are not necessarily typical, they do reflect real crustal
407 structure.

408

409 *Stacked receiver functions*

410

411 Stacked receiver functions at each station are plotted on cross-sections
412 across Sabah (Figure 2). Cross-section A (Figure 2 (a)) cuts through the
413 highest topography in Sabah in the region around Mt Kinabalu. Heading SE
414 from the NW coast there is a positive arrival that decreases from ~4.5 s to ~3
415 s delay time at the stations immediately beneath the highest topography.
416 Moving further SE, the delay time of this prominent positive arrival then
417 increases to ~7 s at station SBE4 (dark grey dashed line). At stations to the
418 SE of Mt Kinabalu, this positive arrival is preceded by a large amplitude
419 negative arrival that similarly shows an increase in arrival time from ~3 s at
420 SBF2 to ~5 s at SBE4 (light grey dashed line). There is a clear change in the
421 character of the receiver functions from ~200 km along the cross section, with
422 the portion of cross-section A between SBD5 and SBD7 having a large
423 amplitude positive arrival at ~6-6.5 s (dark grey dashed line).

424

425 In cross-section B (Figure 2 (b)), the stations in the Crocker Range have a
426 relatively consistent large amplitude positive arrival (dark grey dashed line) at
427 ~4 s, while at SBB3 and SBD4, immediately to the SE, the largest amplitude
428 positive arrival appears to be at ~6.5 s. Between these stations and those in
429 the vicinity of the Maliau Basin there is a strong positive arrival at ~3.5 s, while
430 at the stations near to the Maliau Basin there is an arrival at ~5 s. At the
431 south-east end of the cross-section, in the Semporna Peninsula, the largest

432 positive arrivals, after the direct P arrival, is again at a shorter delay time of
433 around 4 s.

434

435 The peak at ~ 0 s should correspond to the direct P arrival; however if there
436 are low-velocity sediments in the uppermost crust the P-to-S conversion from
437 the base of these may interfere with the direct P resulting in the first positive
438 arrival being shifted away from 0 s. This is observed at several sites,
439 e.g., SBD6 (Figure 2 (a)) and MALB (Figure 2 (b)) and is anticipated given the
440 thick sedimentary basins (>6 km sediments, Hall, 2013) in Sabah.

441

442 *Shear velocity structure*

443

444 Using the 1-D shear wave velocity model beneath each station, 2D,
445 composite velocity cross sections have been constructed using bicubic
446 interpolation for several lines across Sabah, taking the velocity models for
447 stations within 50km of the line. The models shown in Figure 3 are derived
448 from the inversions that used $p=0.1$ and the 3.7 km/s starting model; however,
449 the features remain consistent with the various weightings and starting
450 models tested. Given the high weight of the receiver functions in the models
451 shown, the descriptions and interpretations of the models are primarily
452 concerned with changes in velocity, and relative velocities, rather than
453 absolute velocities. The orientations of cross-sections A and B are chosen to
454 be approximately perpendicular to the strike of the Crocker range, while
455 cross-sections C, D, and E are chosen to help further elucidate the 3D crustal
456 structure.

457 In cross-section A (Figure 3(a)), low velocity sedimentary basins, labelled as 1
458 in the cross-section, are illuminated offshore to the NW (SBG1) and in the
459 south-eastern half of the cross-section (SE of SBE4), confirming the
460 observation of a broadened, delayed P arrival in the receiver function stacks.
461 Low velocities extend to depths of ~10 km. The most striking feature of this
462 cross-section is a dipping high velocity layer, labelled 2, extending from SBE3
463 to SBE5 from ~5 km to 50 km depth, with a dip in the cross section to the SE,
464 which overlies a low velocity layer, labelled 3, with a similar dip. This fits the
465 pattern of arrivals seen in the receiver function cross-sections: a seemingly
466 dipping transition from a high velocity to a low velocity layer resulting in a
467 negative arrival, followed by a low to high velocity discontinuity with increasing
468 depth.

469 In cross-section B (Figure 3(b)) low velocities, labelled 4, are also observed to
470 ~10 km depth in the vicinity of known sedimentary basins between SBC4 and
471 SBA7. The transition to mantle velocities ($\sim >4.2$ km/s in this model) occurs at
472 ~30-35 km depth in the north-western part of the cross section but deepens to
473 greater than 40 km beneath SBC4. It shallows to ~25 km beneath SBB4 and
474 SBC5, before deepening to ~35 km again beneath the Maliau Basin. This
475 agrees with the pattern of positive arrivals observed in the stacked receiver
476 functions, with those for stations between the Crocker Range and the Maliau
477 Basin experiencing the shortest delay times. At the southeast end of cross-
478 section B, the crust beneath SBA8 and SBA9 has lower velocities (~ 3.9 km/s
479 in this model) at the gradient interpreted to be the Moho, labelled 5, than
480 beneath stations elsewhere in the section.

481

482 The differences in crustal structure from south to north through western
483 Sabah is highlighted in cross-section C (Figure 3(c)). The crustal structure at
484 the north-east end of this section, to the north of Mt Kinabalu, has a different
485 character to that in the central portion of the section (between SBD2 and
486 SBE3). In the north east, very high velocities (>4.2 km/s in this model),
487 labelled 6, are observed at ~ 20 km, while in the central portion they are
488 generally low (<3.4 km/s in this model) at this depth in a somewhat
489 discontinuous layer, labelled 7, likely the dipping low velocity layer observed
490 in cross-section A. Cross-section D (Figure 3(d)) cuts to the east of the
491 Crocker Range, through the Maliau Basin. In the south west of this section
492 there is a northeasterly dipping transition from crust to mantle velocities (~ 4.2
493 km/s in this model) from 25 to 45 km depth between SBA3 and the Maliau
494 Basin. At SBC5 it decreases sharply to a depth of 25 km, the depth it is also
495 observed to be at between SBE4 and SBF4. Beneath SBD4 relatively high
496 velocities are observed in the upper crust, labelled 8, and low velocities are
497 observed between 25 and 45km depth. This location corresponds with where
498 ophiolitic material is found on the surface around Telupid (e.g. Hall 2013) . In
499 the south of cross-section E (Figure 3(e)), which cuts through the Semporna
500 and Dent Peninsulas, the transition between crustal and mantle velocities at
501 ~ 35 km depth is relatively gradual. This contrasts with further north, where this
502 transition is sharper, and upper mantle velocities are faster.

503

504 *Moho depth*

505

506 The depth of the Moho beneath each station is picked from its corresponding
507 1-D shear velocity model at the depth that corresponds to the base of the
508 steepest positive velocity gradient where shear velocity exceeds 4 km/s
509 (Figure 4). The depth of the Moho is found to vary from 24 km at SBC6 and
510 SBF4 to 60 km at MTM, although most other measurements are <48 km. The
511 deepest Moho is found in a SW-NE trending band on the eastern edge of the
512 Crocker Range, where the Moho depth exceeds 40 km. It is also relatively
513 deep (40-44 km) beneath the Maliau Basin and beneath other circular basins
514 to the north of the Maliau Basin, and to the west of the Segama ophiolite. The
515 shallowest Moho depth (24-26 km) is found in a band between the Crocker
516 Range and the circular basins, with changes in Moho depth of ~15-25 km
517 occurring over short lateral distances (~20 km).

518

519 At the stations marked with white hexagons in Figure 4, it was not clear where
520 the Moho should be picked. For instance, at a subset of stations (e.g., SBD6,
521 SBD7, and SBC8) there is a very gradual increase in velocities over a wide
522 (~40 km) depth range (Supplementary Figure 7), while at other stations (e.g.,
523 SBD5, SBE4, and SBG3) the models have two steep velocity gradients, both
524 of which could represent plausible Moho locations given those found
525 elsewhere in Sabah, for example at 28km and 58km for SBD5.

526

527 **Discussion**

528

529 *Limitations of the models*

530

531 The 1D velocity models obtained in the study have a number of limitations,
532 which should be acknowledged in order to avoid over interpretation of the
533 results. The receiver functions used in the inversions are single stacks for
534 each station. This is done to reduce noise and source effects, however it may
535 mask real complexity in crustal structure such as short-length scale lateral
536 variations, anisotropy and dipping layers, which we have not be able to model
537 due to the limitations imposed by the backazimuthal range of the events.
538 Therefore it is likely that crustal structure beneath Sabah is more complex
539 than shown in the models here.

540

541 In the inversions we use the relatively coarse, global model, GDM52
542 (Ekstrom, 2011), to help ensure the shear velocities are reasonable for the
543 regional context. While the fits to the dispersion curves are reasonably good
544 (Supplementary Figure 4), the focus of this study is the constraints provided
545 by the radial P wave receiver functions, and so we prioritise the fit to the
546 receiver functions for the models that we interpret. As the models are strongly
547 weighted to the receiver functions, this means that the best constrained
548 features in the crustal structure will be the velocity discontinuities, such as the
549 Moho, rather than absolute velocities. In not using the dispersion
550 measurements from Fone et al., (2024) and Greenfield et al., (2022), we are
551 able to obtain an independent image of crustal structure, and thus make
552 comparisons between the models, giving insight into the robustness of
553 individual features and their potential interpretations.

554

555 *Processes affecting crustal thickness*

556

557 It is important to account for the effect of the interference between
558 conversions and multiples (e.g., Gilligan et al., 2014): a consequence is that
559 the largest signal on a receiver function should not necessarily be interpreted
560 as being due to the velocity increase at the Moho. However, there is a
561 consistent pattern between the positive arrivals observed in the stacked
562 receiver functions and the velocity changes at the Moho observed in the
563 models from joint inversion, suggesting that the receiver functions can, in this
564 instance, provide an interpretable picture for trends in Moho depth.

565

566 The variations in crustal thickness across Sabah observed in this study are in
567 general agreement with the estimates made by recent studies using 2-plane-
568 wave tomography (Greenfield et al., 2022) and virtual deep seismic sounding
569 (Linang et al., 2022): central Sabah appears to have significantly thinner crust
570 than that beneath the Crocker Range and the Circular Basins (Supplementary
571 Figure 8). One notable difference with the Greenfield et al., (2022) Moho
572 estimate is beneath the Semporna Peninsular they observe thick crust
573 (>55km), while in this study we observe crustal thickness of ~34km. This
574 difference is likely to arise due to Greenfield et al., (2022) using the 4.1km/s
575 shear velocity contour as a proxy for Moho depth, and this, as discussed
576 below, may not be an appropriate velocity proxy for the lower crust/upper
577 mantle beneath the Semporna Peninsular.

578

579 The pattern of thicker and thinner crust broadly agrees with the estimates of
580 Holt (1998) using gravity data; however, between the Crocker Range and
581 thickened crust beneath the circular basins we observe a significantly thinner

582 crust (e.g., 25 and 24 km at SBC5 and SBC6 respectively) than the 32 km
583 suggested by Holt (1998). Modelling gravity data is notoriously non-unique,
584 and Holt (1998) uses a very simple model for crustal densities. Given the lack
585 of other constraints on the properties of the crust at the time this may have
586 been appropriate; however, the lateral and vertical heterogeneity of the crust
587 demonstrated in this study indicates a more complex model is required, which
588 may alter the estimates of crustal thickness from the gravity data.

589

590 It should be noted that the crust in this study is thicker throughout much of
591 Sabah than was shown in interpretative cross-section of Hall (2013), which
592 bases Moho depth off the results of Holt (1998), modified for denser material.
593 Hall (2013)'s cross-section shows a maximum Moho depth of 40 km beneath
594 the Crocker Range, and around 20 km beneath both the circular basins and
595 the Dent and Semporna peninsulas. Further, our estimates of crustal
596 thickness shows a significantly different pattern and depths to the estimates
597 made by Tang and Zheng (2013). They report crustal thicknesses of ~27.5 to
598 32.5 km, increasing southward across Sabah, based on the depth of the 4
599 km/s velocity contour in their shear velocity model. This model encompasses
600 the whole of the South China Sea and surrounding region and, as such, has
601 more limited resolution in Sabah compared to this study and others
602 (Greenfield et al., 2022, Linang et al., 2022) that have used the data from the
603 nBOSS network. The thicker crust we observe, compared to earlier estimates,
604 may mean that there is a larger contribution from regional tectonic shortening
605 to the regional uplift observed by Roberts et al., (2018).

606

607 The relatively thick crust (>40 km) beneath the Crocker Range, particularly on
608 the eastern side, is likely to have been thickened during the Sabah Orogeny
609 (~23 Ma), when the Dangerous Grounds block collided with the western edge
610 of northern Borneo at the final stage of the subduction of the proto-South
611 China Sea (e.g., Hutchison et al., 2000, Hall 2013, Rangin et al., 1999). The
612 velocity discontinuity picked as the Moho for many stations in the Crocker
613 Range is the base of the SE dipping slow velocities seen in cross-section A,
614 which we interpret as the base of the underthrust Dangerous Grounds crust.
615
616 Extension, related to the roll-back of the Celebes Sea slab (e.g., Hall, 2013),
617 could have thinned the crust in central Sabah to 20-25 km. Indeed, Tsikouras
618 et al. (2021) argue that the basalts they date to 9-10 Ma in the Telupid area,
619 are rift-related, thus implying significant extension and crustal thinning,
620 although this is disputed by Cullen and Burton-Johnson (2021). A double
621 discontinuity is observed in our study in the 1-D velocity models at some
622 stations (e.g., SBE4), and could indicate that it may not necessarily be
623 appropriate to simply interpret the velocity gradient at ~20-25 km as a single
624 Moho. If the crust is 20-25 km thick, the question as to the extent to which this
625 crust may have been thinned remains, i.e., what was the pre-extensional
626 crustal thickness? Greenfield et al. (2022) assume that it was 40-50 km, as is
627 observed beneath the Crocker Range and circular basins, and thus calculate
628 a stretching factor of 1.3-2. However, if this area was not significantly
629 thickened during the Sabah Orogeny, which is plausible given the lack of
630 underthrust Dangerous Grounds material observed in this study, then pre-
631 extensional thickness may have been less to begin with.
632

633 Related to the question of pre-extensional thickness is whether the ~45 km
634 thick crust observed beneath the Maliau Basin and other circular basins is a
635 result of thickening during the Sabah orogeny (~23 Ma). After thickening it
636 may have been separated from other thickened crust beneath the Crocker
637 Range as a result of extension (e.g., in a crustal scale boudinage process as
638 suggested by Linang et al. (2022)). Alternatively, the crust may have been
639 thickened at a later point in time. Tongkul and Chang (2003) suggest that
640 eastern Sabah experienced N-S compression in the mid Middle Miocene (~13
641 Ma), which led to the segmentation of the large basin in eastern Sabah that
642 had been active in the Early Miocene, and NW-SE compression in the late
643 Upper Miocene (~7-5 Ma), which enhanced the circular shape of the basins,
644 with a period of sediment deposition in between these two compressional
645 events. It may be that during these compressional episodes, potentially
646 associated with Celebes Sea subduction, some crustal thickening occurred
647 beneath the circular basins. More recently, Meju et al., (2024), using results
648 from a magnetotelluric study, argue for thick-skinned deformation and deep
649 crustal flow being involved with the evolution of Neogene 'mini-basins'
650 offshore, which may be directly related to the onshore circular basins such as
651 the Maliau Basin.

652

653 While areas of the highest topography may be anticipated to have some of the
654 thickest crust, intriguingly beneath the stations in the vicinity of the 4095m
655 high Mt Kinabalu the crust is only 30-35km thick. The Kinabalu Granite was
656 emplaced between 7.2-7.8Ma (Cottam et al., 2013), well after the termination
657 proto-South China Sea subduction, thus it would be expected that the crust in

658 this region would have been thickened as a result of this collision. The
659 thermomechanical modelling of Pilia et al., (2023b) shows that as a result of a
660 downwelling drip, e.g the Semporna drip, a region of initially thick crust can be
661 thinned. This thinning could facilitate melting of the lower crust, thus it may be
662 that both the presence of the Kinabalu pluton and the thinner-than-anticipated
663 crust we observe can both be explained by part of the lithosphere having
664 dripped off beneath the Semporna peninsula.

665

666 *Crustal structure*

667

668 Given the diversity of the surface geology in Sabah, it is unsurprising that the
669 crust shows considerable variation. The key elements of our interpretation are
670 shown in Figure 5.

671

672 With the caveat that we have projected 1D velocity models from 50km around
673 the lines of section, and thus may be masking some of the lateral variation
674 perpendicular to this line, we interpret the low velocity (<3.4 km/s in our
675 model) layer seen dipping to the south east from the west coast of Sabah to
676 the eastern edge of the Crocker Range in Cross-section A (Figure 3(a)) as
677 Dangerous Grounds material that has been underthrust beneath Sabah.
678 Underthrusting of attenuated Dangerous Grounds crust has been proposed as
679 the mechanism by which subduction of the proto-SCS stopped (e.g., Hall,
680 2013, Morley and Back, 2008, Hutchison, 2000). Fone et al., (2024) also
681 observe low shear velocities at ~30km depth along a similar line of section,
682 but this is arguably the first time it has been imaged as a dipping structure.

683 Cross-section B (Figure 3(b)), which cuts to the south of Cross-section A, also
684 has a low velocity layer at depths of 20-25 km. In this instance this layer does
685 not seem to dip. We consider this to also be underthrust Dangerous Grounds
686 crust, although this suggests potential along strike variation in the nature of
687 the collision between Sabah and the Dangerous Grounds. Rangin et al.
688 (1999), considering the whole of the proto-SCS, argue that the proto-SCS
689 basin was narrower off the coast of Borneo than the Sulu Sea, and it may be
690 that the differences we observe in underthrust Dangerous Grounds crust are a
691 manifestation of this. Furthermore, Greenfield et al., (2022) note that the
692 lithosphere is thinner in the southwest of Sabah, again suggesting that
693 different processes may have influenced this area compared to those further
694 north.

695

696 Overlying the low-velocity layer in Cross-section A is a high velocity layer,
697 also dipping to the south east, with velocities exceeding 4 km/s in our model
698 in what is interpreted as the upper- to mid-crust. High velocities overlying the
699 lower velocities are also observed by Fone et al., (2024). The velocities we
700 observe are consistent with this being mafic to ultramafic material, although,
701 as noted above, the velocities in our models should primarily be interpreted
702 relatively due to the high weight of receiver function observations in the
703 inversion. However, as this high velocity layer appears to lie beneath areas of
704 peridotitic rocks near Ranau and ophiolitic rocks near Telupid, we interpret the
705 layer as obducted ophiolitic material. It is not possible to constrain the timing
706 of the emplacement from this study, e.g., it may be the result of late Mesozoic

707 rifting (Tsikouras et al., 2021), or it could have been emplaced earlier (e.g.,
708 Cullen and Burton-Johnson 2021).
709
710 The crustal structure of the northern tip of Sabah (to the north of SBF2) is
711 distinct from areas to the south, as is particularly seen in Cross-section C
712 (Figure 3(c)), suggesting that distinct geological processes have shaped this
713 region. As similar structure is seen by Fone et al., (2024), this gives us
714 confidence that this is real structure, given that two independent, but
715 complementary, methods have obtained similar results. The change in the
716 character of the crustal structure is in the same place where there is a change
717 in strike of the surface geology, from ~SW-NE to the south to ~WNW-ESE in
718 the north (Tongkul 1990), in the vicinity of Mt Kinabalu. Moreover, it is
719 approximately coincident with where the fast velocity anomaly in the upper
720 mantle that Pilia et al. (2023a) associate with the proto-South China Sea slab
721 terminates. Tongkul (1994) suggests, based on the relationships between
722 sedimentary rocks in this region, that the basement here - Mesozoic oceanic
723 crust - is uplifted relative to the area to the south. Tongkul (1994) further
724 suggests that this region was affected by the collision with the Reed Bank,
725 resulting in N-S compression, while further south the collision was with the
726 Dangerous Grounds block. Gozzard et al., (2018) observe that the crust
727 beneath the Reed Bank has not been thinned in the same way as the
728 Dangerous Grounds block. Franke et al., (2008) also note the presence of the
729 Kudat block off the eastern shore of northernmost Sabah, which active source
730 seismic data suggests has a different crustal structure. It may be that the
731 different properties of blocks colliding with Sabah, as well as the orientation of

732 the collisions, resulted in the contrasting crustal structure we observe today:
733 underthrust material to the south but not at the northern tip of Sabah.
734
735 In the east of Sabah, the lower crust and upper mantle beneath stations in the
736 Semporna Peninsula (SBA8 and SBA9) is relatively slow (~3.8-4 km/s for the
737 uppermost mantle compared to 4.3-4.5 km/s elsewhere). This is similar to the
738 results from the two-plane wave tomography of Greenfield et al. (2022).
739 Volcanism in this area occurred until at least 0.2 Ma (Lai et al., 2021) and
740 potentially as recently as 24-27 ka (Kirk, 1968; Bellwood, 1988; cited in Tjia et
741 al., 1992) with hot springs found in the vicinity of Tawau today, with water
742 temperatures of up to 75°C (Siong et al., 1991). Pilia et al. (2023b) and
743 Greenfield et al. (2022) propose that part of the lithosphere has been removed
744 beneath the Semporna Peninsula and has been replaced by hot
745 asthenospheric material. This would mean that the remaining crust and
746 mantle would be expected to be warm and thus seismically slow, as we
747 observe here.

748

749

750

751 **Conclusion**

752

753 We present a high-resolution crustal shear velocity model of Sabah, northern
754 Borneo, from the joint inversion of P receiver functions and surface wave
755 data. We image, for the first, time dipping Dangerous Grounds crust
756 underthrust beneath most of the Crocker Range. This has had the effect of

757 thickening the crust beneath the present-day mountain range, with crustal
758 thicknesses exceeding 40 km. However, beneath Mt Kinabalu, crustal
759 thicknesses are only in the range 30-35km, supporting earlier ideas (Cottam
760 et al., 2013, Sapin et al., 2013, Tsikouras et al., 2021, Pilia et al., 2023b) that
761 some degree of crustal thinning may have been involved in its emplacement.
762 Thinner crust (~25 km) between the Crocker Range and the Circular Basins
763 may be due to extension related to the rollback of the Celebes Sea slab (Hall,
764 2013), although the amount of extension remains unclear given that pre-
765 extensional crustal thickness remains unknown. Thicker crust (>40 km)
766 beneath the Maliau and other circular basins suggests that these areas have
767 experienced some degree of crustal thickening, which given the late-mid
768 Miocene age of the sediments that have been deformed is likely to have
769 occurred later than the ~21 Ma Sabah Orogeny. Relatively slow velocities in
770 the lower crust and upper mantle beneath the Semporna Peninsula support
771 work by Pilia et al. (2023b) and Greenfield et al. (2021) that lithospheric
772 delamination has occurred here.

773

774 Overall, we observe a high degree of heterogeneity in the crustal structure
775 beneath Sabah, on length scales of 10s of kilometres. This highlights the
776 complexity of subduction, collisional, post-subduction, and extensional
777 processes that have shaped Sabah over the Cenozoic, and reinforces the
778 importance of dense instrumentation in order to better understand tectonic
779 activity that has occurred in similar settings.

780

781 **Global Research Collaboration Statement**

782 Thanks to all those who were involved in the deployment, servicing and
783 recovery of the nBOSS network between March 2018 and January 2020.
784 Many thanks to the landowners throughout Sabah who hosted seismometers
785 on their property. We thank MetMalaysia for providing access to their
786 restricted continuous waveform data recorded by their permanent MY network
787 in Sabah. Fieldwork was conducted under a Research Pass from the
788 Economic Planning Unit (EPU) of the Malaysian Government for the project
789 “North Borneo Uncovered: Orogenic Processes at a Post-Subduction
790 Continental Margin.”

791

792

793 **Acknowledgements**

794

795 Seismometers used in the nBOSS network were provided by the University of
796 Cambridge, the University of Aberdeen (Aberdeen University Geophysical
797 Equipment Repository – AUGER), and the Natural Environment Research
798 Council (NERC) Geophysical Equipment Facility through SeisUK (loan 1038).
799 A.G was supported by a Royal Astronomical Society Independent Research
800 Fellowship. S. P was supported by the Natural Environmental Research
801 Council (NERC) Grant NE/R013500/1 and from the European Union's Horizon
802 2020 Research and Innovation Program under Marie Skłodowska-Curie Grant
803 Agreement 790203. T.G. was supported by an Early Career Fellowship from
804 the Leverhulme Trust. We have made use of several open source Python
805 packages in our analysis and visualisation, including Matplotlib (Hunter,
806 2007); and ObsPy (Beyreuther et al., 2010). A number of figures were

807 produced using the Generic Mapping Tools version 6 (Wessel et al.,
808 2019). We thank Robert Herrmann for making the Computer Programs in
809 Seismology freely available.

810

811 **Data availability**

812

813 The nBOSS dataset is accessible through the EarthScope Data Management
814 Center (https://www.fdsn.org/networks/detail/YC_2018/). Data from the
815 Malaysian national seismic network
816 (<https://www.fdsn.org/networks/detail/MY/>) are restricted but may be obtained
817 by contacting the Malaysian Meteorological Department. The exceptions to
818 this are stations KKM and LDM which are also available through the
819 Earthscope Data Management Center. The Open Science Framework site for
820 this project, which includes figures for each station analysed, and SAC files
821 for the receiver functions used can be found at: <https://osf.io/2zvvcg/>

822

823 **Author contributions**

824

825 **A.G.:** Formal analysis, conceptualisation, funding acquisition, investigation,
826 resources, visualisation, writing – original draft; **D.C.:** Investigation, resources,
827 writing - review and editing; **N.R.:** Conceptualisation, funding acquisition,
828 resources, investigation, writing – review and editing; **F.T.:** Conceptualisation,
829 resources, investigation; **S.P.:** Investigation, writing – review and editing,
830 funding acquisition; **T.G.:** Investigation, writing – review and editing; **C.B.:**
831 Data curation, investigation.

832

833 **References**

834

835 Amaru, M. L. (2007). *Global travel time tomography with 3-D reference models* (Vol. 274).
836 Utrecht University.

837

838 Ammon, C. J., Randall, G. E., & Zandt, G. (1990). On the nonuniqueness of receiver function
839 inversions. *Journal of Geophysical Research: Solid Earth*, 95(B10), 15303-15318.

840

841 Bacon, C. A. (2021). *Seismic anisotropy and microseismicity: from crustal formation to*
842 *subduction termination*, University of Cambridge (United Kingdom)

843

844

845 Bacon, C. A., Rawlinson, N., Pilia, S., Gilligan, A., Wehner, D., Cornwell, D. G., & Tongkul, F.
846 (2022). The Signature of Lithospheric Anisotropy at Post-Subduction Continental Margins:
847 New Insight From XKS Splitting Analysis in Northern Borneo. *Geochemistry, Geophysics,*
848 *Geosystems*, 23(11), e2022GC010564.

849

850 Balaguru, A., & Nichols, G. (2004). Tertiary stratigraphy and basin evolution, southern Sabah
851 (Malaysian Borneo). *Journal of Asian Earth Sciences*, 23(4), 537-554.

852

853 Barckhausen, U., Engels, M., Franke, D., Ladage, S., & Pubellier, M. (2014). Evolution of the
854 South China Sea: Revised ages for breakup and seafloor spreading. *Marine and Petroleum*
855 *Geology*, 58, 599-611.

856

857 Bellwood, P. S. (1988). Archaeological research in south-eastern Sabah. Sabah Museum and
858 State Archives

859

860 Beyreuther, M., Barsch, R., Krischer, L., Megies, T., Behr, Y., & Wassermann, J. (2010).
861 ObsPy: A Python toolbox for seismology. *Seismological Research Letters*, 81(3), 530-533.

862

863 Bird, P. (2003). An updated digital model of plate boundaries. *Geochemistry, Geophysics,*
864 *Geosystems*, 4(3).

865

866 Burton-Johnson, A., Macpherson, C. G., Muraszko, J. R., Harrison, R. J., & Jordan, T. A.
867 (2019). Tectonic strain recorded by magnetic fabrics (AMS) in plutons, including Mt Kinabalu,
868 Borneo: A tool to explore past tectonic regimes and syn-magmatic deformation. *Journal of*
869 *Structural Geology*, 119, 50-60.

870

871 Burton-Johnson, A., Macpherson, C. G., Millar, I. L., Whitehouse, M. J., Ottley, C. J., &
872 Nowell, G. M. (2020). A Triassic to Jurassic arc in north Borneo: Geochronology,
873 geochemistry, and genesis of the Segama Valley Felsic Intrusions and the Sabah
874 ophiolite. *Gondwana Research*, 84, 229-244.

875

876 Burton-Johnson, A., & Cullen, A. B. (2023). Continental rifting in the South China Sea through
877 extension and high heat flow: An extended history. *Gondwana Research*, 120, 235-263

878

879

880 Cottam, M. A., Hall, R., Sperber, C., Kohn, B. P., Forster, M. A., & Batt, G. E. (2013).
881 Neogene rock uplift and erosion in northern Borneo: evidence from the Kinabalu granite,
882 Mount Kinabalu. *Journal of the Geological Society*, 170(5), 805-816.

883

884 Cullen, A., & Burton-Johnson, A. (2021). [Comment] New zircon radiometric U-Pb ages and
885 Lu-Hf isotopic data from the ultramafic-mafic sequences of Ranau and Telupid (Sabah,
886 eastern Malaysia): Time to reconsider the geological evolution of Southeast
887 Asia?. *Geology*, 49(11), 541-541.

888

889 Forsyth, D., & Uyeda, S. (1975). On the relative importance of the driving forces of plate
890 motion. *Geophysical Journal International*, 43(1), 163-200.

891
892 Franke, D., Barckhausen, U., Heyde, I., Tingay, M., & Ramli, N. (2008). Seismic images of a
893 collision zone offshore NW Sabah/Borneo. *Marine and Petroleum Geology*, 25(7), 606-624.
894
895 Ekström, G. (2011). A global model of Love and Rayleigh surface wave dispersion and
896 anisotropy, 25-250 s. *Geophysical Journal International*, 187(3), 1668-1686.
897
898 Foley, S., Tiepolo, M., & Vannucci, R. (2002). Growth of early continental crust controlled by
899 melting of amphibolite in subduction zones. *Nature*, 417(6891), 837-840.
900
901 Fone, J. W., Rawlinson, N., Pilia, S., Gilligan, A., Cornwell, D., & Tongkul, F. (2024). Ambient
902 noise tomography of northern Borneo reveals evidence of subduction and post-subduction
903 processes. *Journal of Geophysical Research: Solid Earth*, 129,
904 e2024JB029092. <https://doi.org/10.1029/2024JB029092>
905
906 Franke, D. (2013). Rifting, lithosphere breakup and volcanism: Comparison of magma-poor
907 and volcanic rifted margins. *Marine and Petroleum geology*, 43, 63-87.
908
909 Gilligan, A., Roecker, S. W., Priestley, K. F., & Nunn, C. (2014). Shear velocity model for the
910 Kyrgyz Tien Shan from joint inversion of receiver function and surface wave
911 data. *Geophysical Journal International*, 199(1), 480-498.
912
913 Gozzard, S., Kuszniir, N., Franke, D., Cullen, A., Reemst, P., & Henstra, G. (2019). South
914 China Sea crustal thickness and oceanic lithosphere distribution from satellite gravity
915 inversion. *Petroleum Geoscience*, 25(1), 112-128.
916
917 Greenfield, T., Gilligan, A., Pilia, S., Cornwell, D. G., Tongkul, F., Widiyantoro, S., &
918 Rawlinson, N. (2022). Post-Subduction Tectonics of Sabah, Northern Borneo, Inferred From
919 Surface Wave Tomography. *Geophysical Research Letters*, 49(3), e2021GL096117.
920
921 Hall, R. (2013). Contraction and extension in northern Borneo driven by subduction
922 rollback. *Journal of Asian Earth Sciences*, 76, 399-411.
923
924 Hall, R., & Spakman, W. (2015). Mantle structure and tectonic history of SE
925 Asia. *Tectonophysics*, 658, 14-45.
926
927 He, K., Zhang, X., Ren, S., & Sun, J. (2016). Deep residual learning for image recognition.
928 In *Proceedings of the IEEE conference on computer vision and pattern recognition* (pp. 770-
929 778).
930
931 Herrmann, R. B. (2013). Computer programs in seismology: An evolving tool for instruction
932 and research. *Seismological Research Letters*, 84(6), 1081-1088.
933
934 Hunter, J. D. (2007). Matplotlib: A 2D graphics environment. *Computing in science &*
935 *engineering*, 9(03), 90-95.
936
937 Hutchison, C. S., Bergman, S. C., Swauger, D. A., & Graves, J. E. (2000). A Miocene
938 collisional belt in north Borneo: uplift mechanism and isostatic adjustment quantified by
939 thermochronology. *Journal of the Geological Society*, 157(4), 783-793.
940
941 Holt, R. A. (1998). *The gravity field of Sundaland-acquisition, assessment and interpretation*.
942 University of London, University College London (United Kingdom)
943
944 Huang, Z., Gradstein, F.M., and Loudon, K.E., (1991). Subsidence and sedimentation
945 analysis of marginal basins: Celebes Sea and Sulu Sea, Leg 124, Sites 767 and 768,
946 in Silver, E.A., Rangin, C., von Braymann, M.T., et al, Proceedings of the Ocean Drilling
947 Program, *Scientific Results*, 124, 399-407
948

949 Johnston, F. K., Turchyn, A. V., & Edmonds, M. (2011). Decarbonation efficiency in
950 subduction zones: Implications for warm Cretaceous climates. *Earth and Planetary Science*
951 *Letters*, 303(1-2), 143-152.
952
953 Kennett, B. L., Engdahl, E. R., & Buland, R. (1995). Constraints on seismic velocities in the
954 Earth from traveltimes. *Geophysical Journal International*, 122(1), 108-124.
955
956 Kirk, H. J. C. (1968). The igneous rocks of the Sarawak and Sabah. *Geological Survey*
957 *Borneo Region, Malaysia, Bull*, 5, 201.
958
959
960 Lai, C. K., Xia, X. P., Hall, R., Meffre, S., Tsikouras, B., Rosana Balangue-Tarriela, M. I., ... &
961 Norazme, N. A. (2021). Cenozoic Evolution of the Sulu Sea Arc-Basin System: An
962 Overview. *Tectonics*, 40(2), e2020TC006630.
963
964 Latiff, A. H. A., & Othman, F. (2020). Earth crustal analysis of Northwest Sabah region
965 inferred from receiver function method. *Warta Geologi*, 46(2), 59-68.
966
967 Levander, A., Schmandt, B., Miller, M. S., Liu, K., Karlstrom, K. E., Crow, R. S., Lee, C.-T. A.,
968 & Humphreys, E. D. (2011). Continuing Colorado plateau uplift by delamination-style
969 convective lithospheric downwelling. *Nature*, 472(7344), 461-465.
970
971 Li, C. F., Xu, X., Lin, J., Sun, Z., Zhu, J., Yao, Y., ... & Zhang, G. L. (2014). Ages and
972 magnetic structures of the South China Sea constrained by deep tow magnetic surveys and
973 IODP Expedition 349. *Geochemistry, Geophysics, Geosystems*, 15(12), 4958-4983.
974
975 Li, Z. H., Liu, M., & Gerya, T. (2016). Lithosphere delamination in continental collisional
976 orogens: A systematic numerical study. *Journal of Geophysical Research: Solid*
977 *Earth*, 121(7), 5186-5211.
978
979 Ligorria, J. P., & Ammon, C. J. (1999). Iterative deconvolution and receiver-function
980 estimation. *Bulletin of the seismological Society of America*, 89(5), 1395-1400.
981
982 Linang, H. T., Pilia, S., Rawlinson, N., Bacon, C. A., Gilligan, A., Cornwell, D. G., & Tongkul,
983 F. (2022). Collision-induced subduction polarity reversal explains the crustal structure of
984 northern Borneo: New results from Virtual Deep Seismic Sounding (VDSS). *Geophysical*
985 *Research Letters*, 49(19), e2022GL099123.
986
987 Lipke, K. (2008). Seismologic investigation of the Sunda arc region with receiver
988 functions. *Potsdam: University of Potsdam*.
989
990 Macpherson, C. G., Chiang, K. K., Hall, R., Nowell, G. M., Castillo, P. R., & Thirlwall, M. F.
991 (2010). Plio-Pleistocene intra-plate magmatism from the southern Sulu Arc, Semporna
992 peninsula, Sabah, Borneo: Implications for high-Nb basalt in subduction zones. *Journal of*
993 *Volcanology and Geothermal Research*, 190(1-2), 25-38.
994
995 Meju, M. A., Saleh, A. S., Karpiah, A. B., Das, P. S., Miller, R. V., Kho, J. H. W., Alleyne,
996 B.G.T., Rice-Oxley, E.D. & Legrand, X. (2024). Upper mantle flow and crustal deformation
997 patterns beneath the Dangerous Grounds and Borneo where multiple plates converge in
998 South China Sea revealed by 3-D anisotropic magnetotelluric imaging. *Geophysical Journal*
999 *International*, 239(3), 1879-1899.
1000
1001 Milsom, J., Holt, R., Hutchison, C. S., Bergman, S. C., Swauger, D. A., & Graves, J. E.
1002 (2001). Discussion of a Miocene collisional belt in north Borneo: uplift mechanism and
1003 isostatic adjustment quantified by thermochronology: *Journal*, Vol. 157, 2000, 783-
1004 793. *Journal of the Geological Society*, 158(2), 396-400.
1005
1006 Morley, C. K., & Back, S. (2008). Estimating hinterland exhumation from late orogenic basin
1007 volume, NW Borneo. *Journal of the Geological Society*, 165(1), 353-366.
1008

1009 Pilia, S., Rawlinson, N., Gilligan, A., & Tongkul, F. (2019). Deciphering the fate of plunging
1010 tectonic plates in Borneo. *Eos, Transactions American Geophysical Union*, 100(10), 18-23.
1011
1012 Pilia, S., Rawlinson, N., Hall, R., Cornwell, D. G., Gilligan, A., & Tongkul, F. (2023a). Seismic
1013 signature of subduction termination from teleseismic P-and S-wave arrival-time tomography:
1014 The case of northern Borneo. *Gondwana Research*, 115, 57-70.
1015
1016 Pilia, S., Davies, D. R., Hall, R., Bacon, C. A., Gilligan, A., Greenfield, T., Tongkul, F., Kramer,
1017 S. C., Wilson, C. R., Ghelichkhan, S., Cornwell, D. G., Colli, L., & Rawlinson, N. (2023b).
1018 Post-subduction tectonics induced by extension from a lithospheric drip. *Nature Geoscience*,
1019 1-7. Rangin, C., Spakman, W., Pubellier, M., & Bijwaard, H. (1999). Tomographic and
1020 geological constraints on subduction along the eastern Sundaland continental margin (South-
1021 East Asia). *Bulletin de la Société géologique de France*, 170(6), 775-788.
1022
1023 Rawlinson, N. (2018). *Northern Borneo Orogeny Seismic Survey* [Data set]. International
1024 Federation of Digital Seismograph Networks. https://doi.org/10.7914/SN/YC_2018
1025
1026 Roberts, G. G., White, N., Hoggard, M. J., Ball, P. W., & Meenan, C. (2018). A Neogene
1027 history of mantle convective support beneath Borneo. *Earth and Planetary Science*
1028 *Letters*, 496, 142-158.
1029
1030 Sapin, F., Hermawan, I., Pubellier, M., Vigny, C., & Ringenbach, J. C. (2013). The recent
1031 convergence on the NW Borneo Wedge—a crustal-scale gravity gliding evidenced from
1032 GPS. *Geophysical Journal International*, 193(2), 549-556.
1033
1034 Schaeffer, A. J., & Lebedev, S. (2013). Global shear speed structure of the upper mantle and
1035 transition zone. *Geophysical Journal International*, 194(1), 417-449.
1036
1037 Siong, L. P., Intang, F., & On, C. F. (1991). Geothermal prospecting in the Semporna
1038 Peninsula with emphasis on the Tawau area. *Geological Society of Malaysia, Bulletin 29*,
1039 135-155
1040
1041 Syuhada, S., Pranata, B., Anggono, T., Ramdhan, M., Zulfakriza, Z., Febriani, F., Prasetio,
1042 A.D., Dewi, C.N., Hasib, M., & Sulaiman, A. (2022). Crustal velocity structure in Borneo Island
1043 using receiver function inversion. *Acta Geophysica*, 70(6), 2529-2553.
1044
1045 Takashima I., Nazri, A. A., Lim, P. S., Koseki, T., Mouri, Y., Nasution, A., & Sucipta, I. E.,
1046 (2004). Thermoluminescence age determination of quaternary volcanic rocks and alteration
1047 products at Tawau area, Sabah, Malaysia. *Journal of the Geothermal Research Society of*
1048 *Japan*, 26(3), 273-283.
1049
1050 Tang, Q., & Zheng, C. (2013). Crust and upper mantle structure and its tectonic implications
1051 in the South China Sea and adjacent regions. *Journal of Asian Earth Sciences*, 62, 510-525.
1052 Tjia, H. D., Komoo, I., Ali, C. A., & Tahir, S. H. (1992). Geology of Taman Bukit Tawau,
1053 Semporna Peninsula, Sabah. *Geological Society of Malaysia, Bulletin 31*, 113-131
1054
1055 Tian, Z., Gao, Y., Wang, P., & Tang, H. (2024). Formation and Tectonic Evolution of
1056 Ophiolites in the Sabah Area (Borneo, SE Asia). *Minerals*, 14(11), 1078.
1057
1058 Tongkul, F. (1990). Structural style and tectonics of Western and Northern Sabah. *Geological*
1059 *Society of Malaysia, Bulletin 27*, 227-239
1060
1061 Tongkul, F. (1991). Tectonic evolution of Sabah, Malaysia. *Journal of Southeast Asian Earth*
1062 *Sciences*, 6(3-4), 395-405.
1063
1064 Tongkul, F. (1994). The geology of Northern Sabah, Malaysia: its relationship to the opening
1065 of the South China Sea Basin. *Tectonophysics*, 235(1-2), 131-147.
1066
1067 Tongkul, F., and Chang, F. K. (2003) Structural geology of the Neogene Maliau Basin, Sabah.
1068 *Geological Society of Malaysia, Bulletin 47*, 51-61

1069
 1070
 1071
 1072
 1073
 1074
 1075
 1076
 1077
 1078
 1079
 1080
 1081
 1082
 1083
 1084
 1085
 1086
 1087
 1088
 1089
 1090
 1091
 1092
 1093
 1094
 1095
 1096

Tsikouras, B., Lai, C. K., Ifandi, E., Teo, C. H., & Xia, X. P. (2021). New zircon radiometric U-Pb ages and Lu-Hf isotopic data from the ultramafic-mafic sequences of Ranau and Telupid (Sabah, eastern Malaysia): Time to reconsider the geological evolution of Southeast Asia?. *Geology*, 49(7), 789-793.

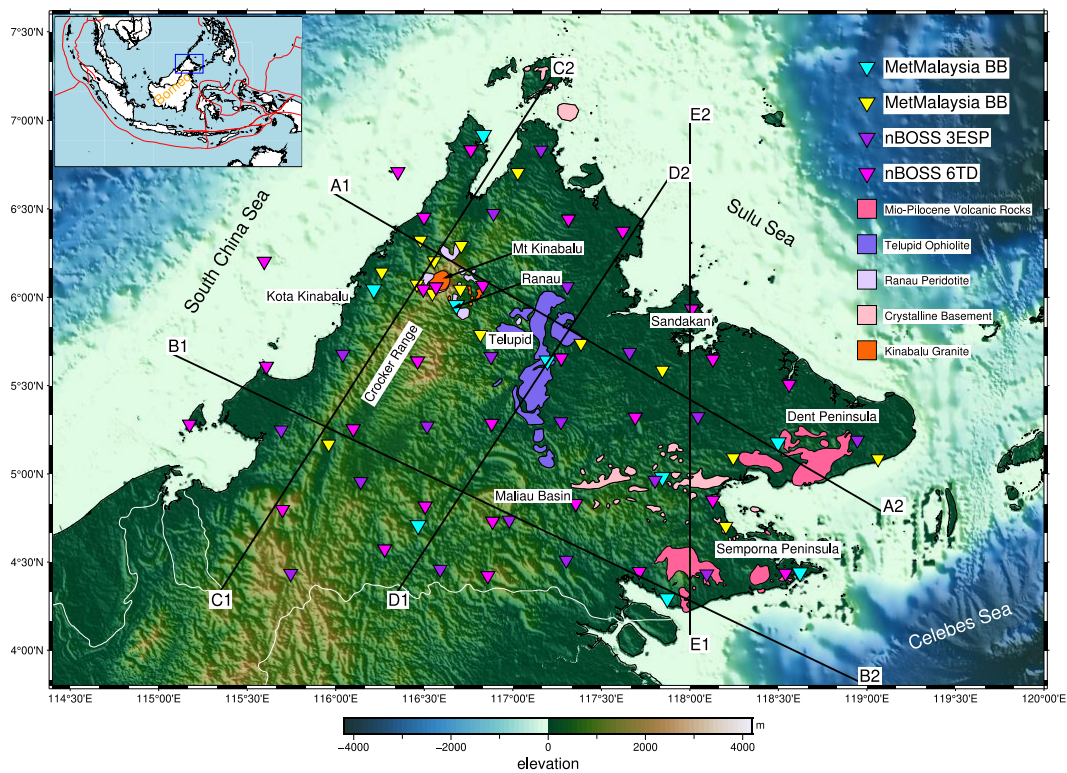
Wehner, D., Blom, N., Rawlinson, N., Böhm, C., Miller, M. S., Supendi, P., & Widiyantoro, S. (2022). SASSY21: A 3-D Seismic Structural Model of the Lithosphere and Underlying Mantle Beneath Southeast Asia From Multi-Scale Adjoint Waveform Tomography. *Journal of Geophysical Research: Solid Earth*, 127(3), e2021JB022930.

Wessel, P., Luis, J. F., Uieda, L., Scharroo, R., Wobbe, F., Smith, W. H., & Tian, D. (2019). The generic mapping tools version 6. *Geochemistry, Geophysics, Geosystems*, 20(11), 5556-5564.

Zandt, G., Gilbert, H., Owens, T. J., Ducea, M., Saleeby, J., & Jones, C. H. (2004). Active foundering of a continental arc root beneath the southern Sierra Nevada in California. *Nature*, 431(7004), 41-46.

Zenonos, A., De Siena, L., Widiyantoro, S., & Rawlinson, N. (2019). P and S wave travel time tomography of the SE Asia-Australia collision zone. *Physics of the Earth and Planetary Interiors*, 293, 106267.

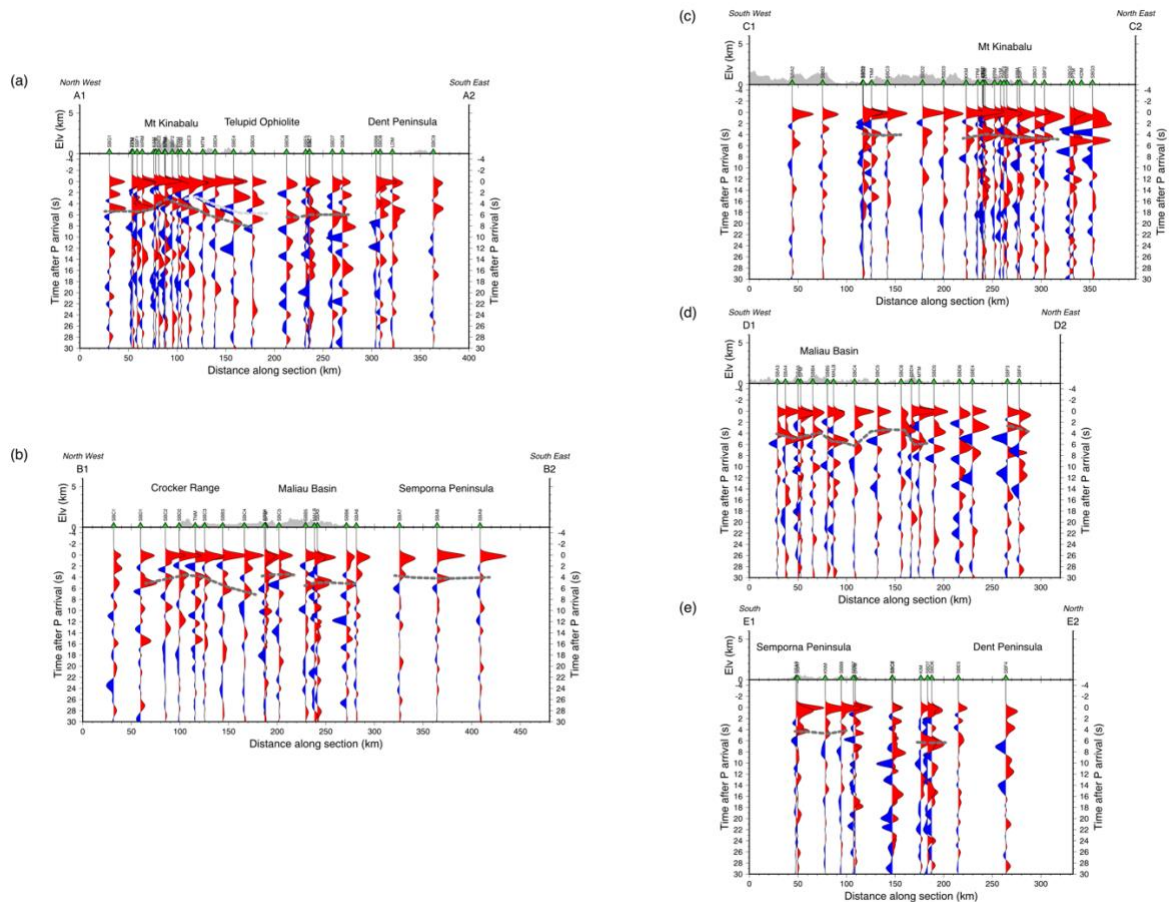
Figures



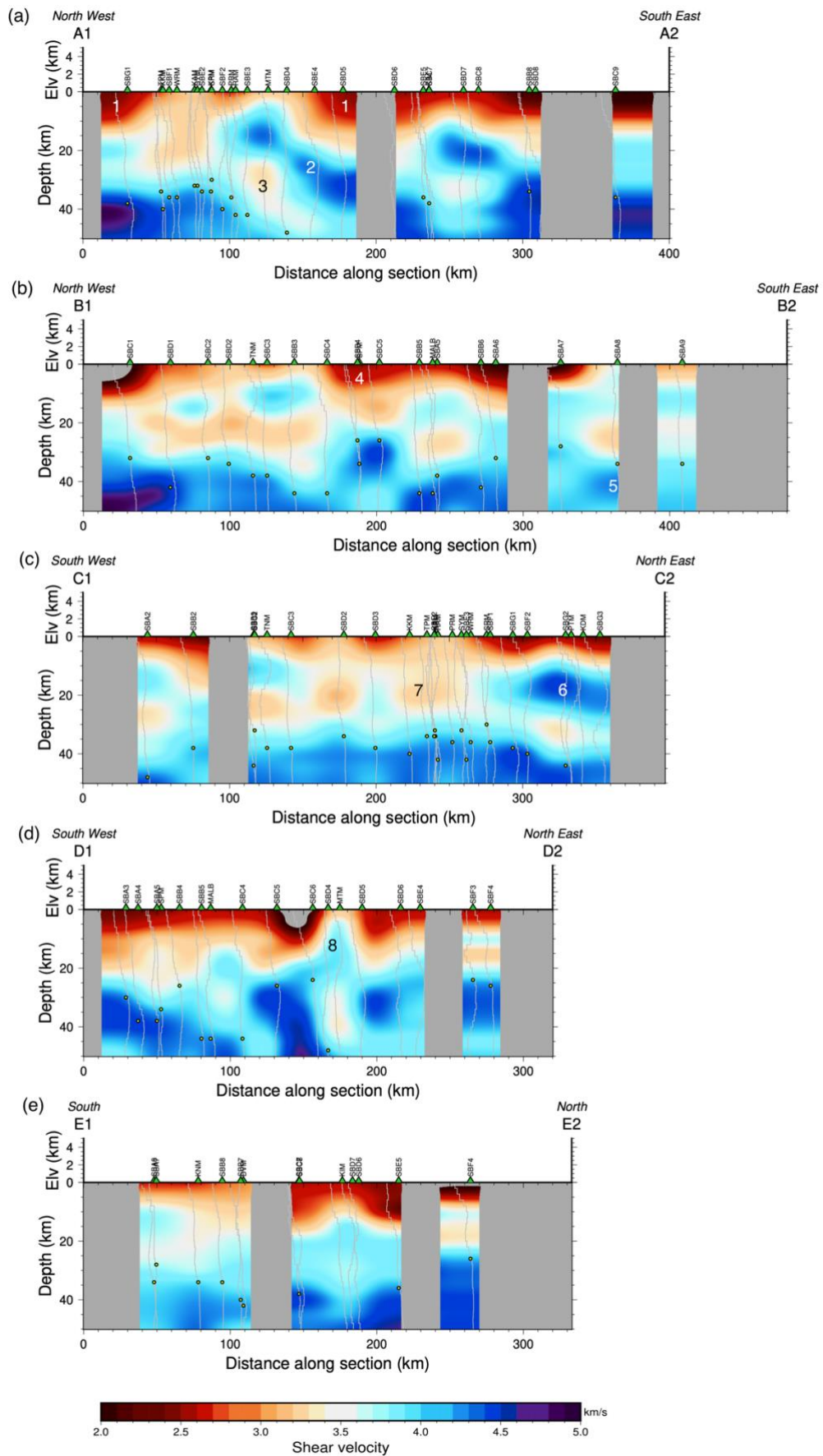
1097
 1098
 1099
 1100
 1101

Figure 1: Map of seismometer stations in Sabah used in this study. Blue triangles are MetMalaysia seismometers deployed before 2017, yellow triangles are MetMalaysia seismometers deployed after 2017. Pink (6TD) and

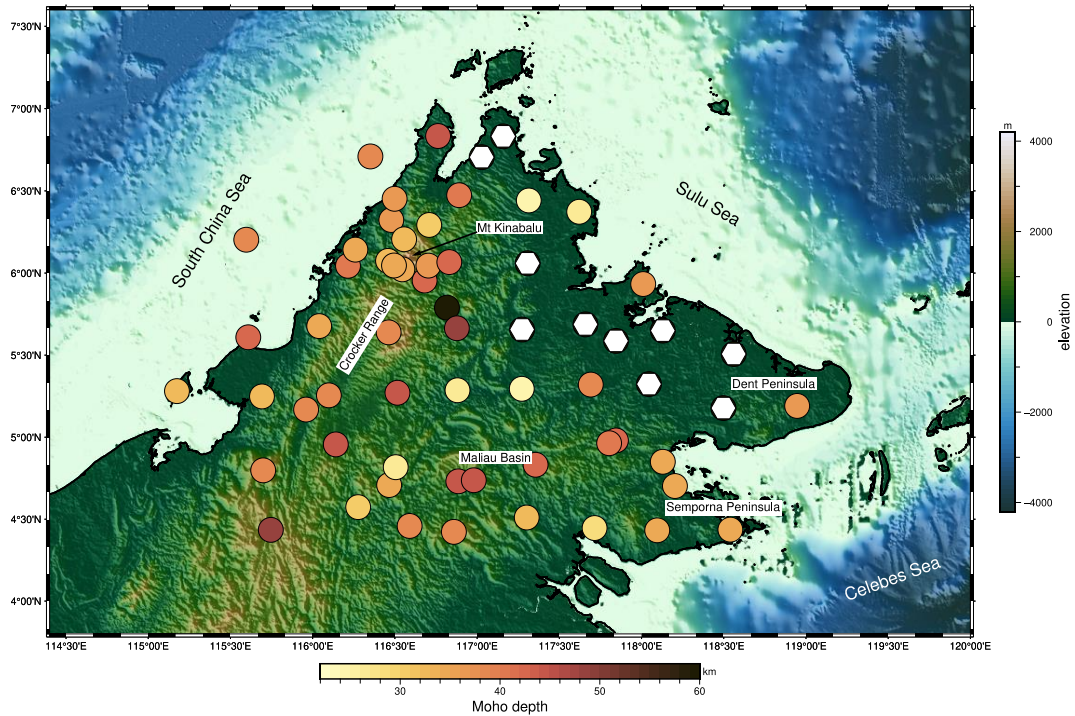
1102 Purple (3ESP) triangles are seismometers deployed as part of the nBOSS
 1103 project. Lines of section are shown: A1-A2 (6.56°N 115.97°E
 1104 4.78°N 119.09°E), B1-B2 (5.691°N 115.05°E - 3.82°N 118.96°E), C1-C2
 1105 (4.25°N 115.30°E - 7.26°N 117.23°E), D1-D2(4.25°N 116.30°E - 6.67°N
 1106 117.88°E) E1-E2 (4°N 118°E - 7°N 118°E). Geological units are plotted after
 1107 Hall (2013). The inset map shows the wider geographical area, with the area
 1108 of the main map highlighted by the blue box, and plate boundaries after Bird
 1109 (2003), are shown by red lines.
 1110
 1111
 1112
 1113



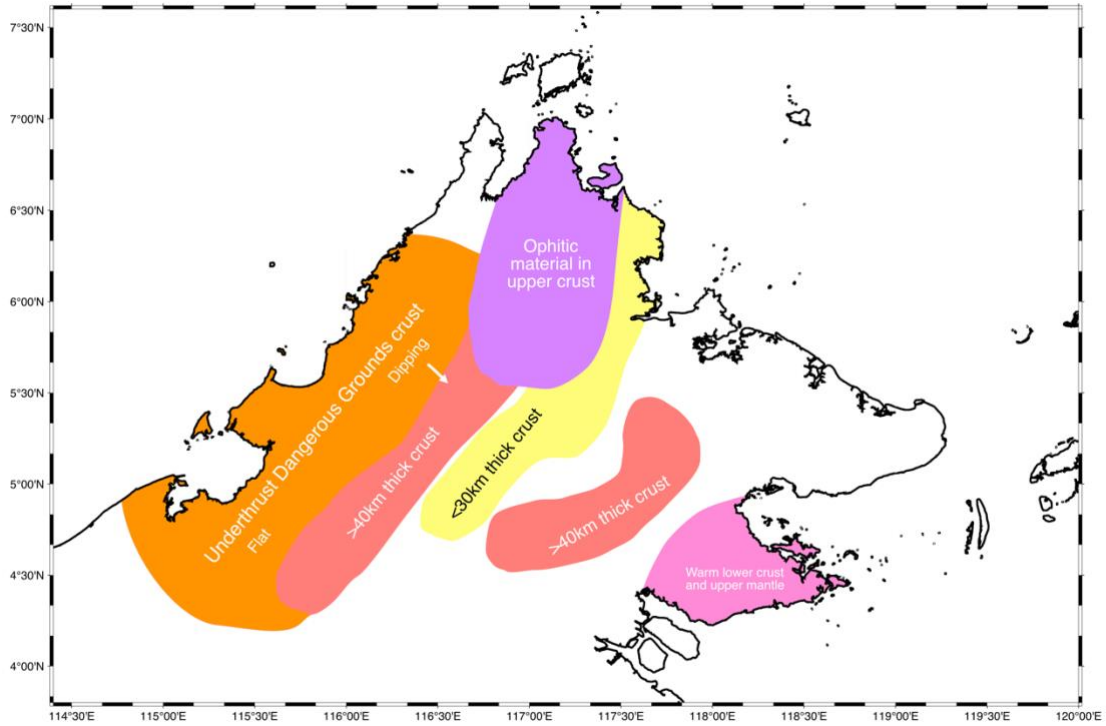
1114
 1115
 1116 **Figure 2:** Stacked receiver functions along the lines (a) A1-A2, (b) B1-B2, (c)
 1117 C1-C2, (d) D1-D2, and (e) E1-E2. Positive arrivals are filled red, and negative
 1118 arrivals are filled blue. In both cases receiver functions from stations within 50
 1119 km of each line have been projected onto the section, along with their
 1120 respective station (green triangles), and topography is plotted above. The
 1121 dark grey dashed line highlights positive arrivals, likely from the P-to-S
 1122 conversion at the Moho. The light grey dashed line highlights negative arrivals
 1123 corresponding to a velocity increase with depth in the crust.



1125 **Figure 3:** Shear velocity vs depth along lines (a) A1-A2, (b) B1-B2, (c) C1-C2,
 1126 (d) D1-D2, (e) E1-E2 from the joint inversion of receiver function and surface
 1127 wave data. 1-D models from stations within 50 km of the line of section are
 1128 interpolated to make the cross-sections. Grey areas indicate areas with no
 1129 station coverage. Green triangles mark the location of stations. Topography
 1130 along the line of section is plotted above. Labelled velocity anomalies 1-8
 1131 are discussed in the text.
 1132
 1133



1134
 1135
 1136 **Figure 4:** Moho depths at seismometer stations in Sabah picked from 1D
 1137 shear velocity models from the joint inversion of receiver function and surface
 1138 wave data. The colour of the circle indicated Moho depth for the station
 1139 located at that point, as shown in the scale. White hexagons are locations
 1140 where there was no clear Moho to be picked or where there were multiple
 1141 plausible velocity discontinuities that could be the Moho.
 1142



1143
 1144
 1145
 1146
 1147
 1148
 1149
 1150
 1151
 1152
 1153
 1154
 1155
 1156
 1157
 1158
 1159
 1160
 1161
 1162
 1163
 1164
 1165
 1166
 1167
 1168
 1169
 1170
 1171
 1172

Figure 5: Summary map highlighting the key interpretations from this study from the shear velocity models derived from the joint inversion of receiver function and surface wave data.